Applied Surface Science 440 (2018) 932–938

Contents lists available at ScienceDirect

Applied Surface Science

journal homepage: www.elsevier.com/locate/apsusc

Full Length Article

Microstructure and thermal stability of $Cu/Zr_{0.3}Al_{0.7}N/Zr_{0.2}Al_{0.8}N/Al_{34}O_{60}N_6$ cermet-based solar selective absorbing coatings

Jian-ping Meng [a,b,d,*], Rui-rui Guo [c], Hu Li [a,b], Lu-ming Zhao [a,b], Xiao-peng Liu [d], Zhou Li [a,b,*]

[a] Beijing Institute of Nanoenergy and Nanosystems, Chinese Academy of Sciences, Beijing 100083, PR China
[b] School of Nanoscience and Technology, University of Chinese Academy of Sciences, Beijing 100049, PR China
[c] China National Energy Investment Group Co., Ltd., Shendong Bo Er Tai Coal Mine, Ordos, Inner Mongolia 017209, PR China
[d] Department of Energy Material and Technology, General Research Institute for Nonferrous Metals, Beijing 100088, PR China

ARTICLE INFO

Article history:
Received 23 October 2017
Revised 24 January 2018
Accepted 29 January 2018
Available online 31 January 2018

Keywords:
Solar selective absorbing coating
High performance
Spinodal decomposition
Phase transition

ABSTRACT

Solar selective absorbing coatings play a valuable role in photo-thermal conversion for high efficiency concentrating solar power systems (CSP). In this paper, a novel $Cu/Zr_{0.3}Al_{0.7}N/Zr_{0.2}Al_{0.8}N/Al_{34}O_{60}N_6$ cermet-based solar selective absorbing coating was successfully deposited by ion beam assisted deposition. The optical properties, microstructure and element distribution in depth were investigated by spectroscopic ellipsometry, UV-vis-NIR spectrophotometer, transmission electron microscope (TEM) and Auger electron spectroscopy (AES), respectively. A high absorptance of 0.953 and a low thermal emittance of 0.079 at 400 °C are obtained by the integral computation according to the whole reflectance from 300 nm to 28,800 nm. After annealing treatment at 400 °C (in vacuum) for 192 h, the deposited coating exhibits the high thermal stability. Whereas, the photothermal conversion efficiency decreases from 12.10 to 6.86 due to the emittance increase after annealing at 600 °C for 192 h. Meanwhile, the nitrogen atom in the $Zr_{0.3}Al_{0.7}N$ sub-layer diffuses toward the adjacent sub-layer due to the spinodal decomposition of metastable *c*-ZrAlN and the phase transition from *c*-AlN to *h*-AlN, which leads to the composition of the $Zr_{0.3}Al_{0.7}N$ sub-layer deviates the initial design. This phenomenon has a guide effect for the thermal-stability improvement of cermet coatings. Additionally, a serious diffusion between copper and silicon substrate also contributes to the emittance increase.

1. Introduction

Solar energy is an important composition in the global clear energy supply [1,2]. There are two main approaches for harvesting energy and generating electricity: photovoltaic (PV) power generation by solar cells and concentrating solar power (CSP) from solar thermal energy [3]. Among the various components in CSP system, solar collector plays a significant role in the overall system performance. The efficiency of solar collector strongly depends on the optical properties of solar selective absorbing coatings, whose function is to maximize the absorption in Vis-NIR region and minimize the thermal emittance in mid- and far-infrared region [4].

A high solar absorptance can be achieved by a gradual decrease of refractive index and extinction coefficient from the metal substrate (infrared reflector) to the surface (anti-reflection layer). In addition, the occurance of destructive interference in visible and near-infrared region will also be able to improve the solar absorptance, which can be obtained by multilayer gradient coating, cermet composite coating and optical interference coating [5–8]. Among those, cermet composite coating with bi-layer structure, located between the metal infrared reflector and dielectric anti-reflectance layer, has been confirmed to possess high absorptance and low emittance [8]. Thus, it becomes the preferred design system. Initially, metal particles as the absorbing unit in metal-dielectric cermet coatings have been developed, such as Ni-NiO [9], $NiCrO_x$ [10], and Mo-SiO_2 [11]. For those coatings, the metal particles are so easy to be oxidized during the preparation and high-temperature applications that its thermal stability or optical properties deteriorates obviously. To improve this issue, the nitrides of transition metals are taken into consideration owing to high melting point, extreme hardness, and outstanding oxidation resistance in consequence of high cohesive energy of *pd* orbital hybridization [12]. Thus, the nitride of transition metals, such as TiN, CrN, ZrN, HfN, NbN, TiON, and CrON, are chosen to as the absorbing units to take place the metal particles. Consequently, a

* Corresponding authors at: Beijing Institute of Nanoenergy and Nanosystems, Chinese Academy of Sciences, Beijing 100083, PR China.
E-mail addresses: mengjianpingallgood@gmail.com (J.-p. Meng), zli@binn.cas.cn (Z. Li).

https://doi.org/10.1016/j.apsusc.2018.01.268
0169-4332/

lot of cermet coatings have been developed [13–18], for instance, the TiAlN combined the TiN (Metal-like materials, absorbing unit) and AlN (dielectric material) is usually designed as the absorbing layer. Whereas, the diffusion of nitrogen and oxygen and oxidation of the metal element also limit its application at 600 °C or higher for long duration service [13,14,18,19].

Zr and Ti are same group element (Group IVB), ZrN and TiN possess some analogical physicochemical properties. What is more, the thermodynamical stability of ZrN ($\Delta H = -365$ kJ/mol) is better than that of TiN ($\Delta H = -336$ kJ/mol), and oxidation activation energy of ZrN (2.5 eV) is higher than that of TiN (2.05 eV) from 500 °C to 650 °C [20,21].

In this paper, ZrN is chosen as the absorbing unit and the AlN as the dielectric matrix for the first to design a new cermet coating of $Cu/Zr_{0.3}Al_{0.7}N/Zr_{0.2}Al_{0.8}N/Al_{34}O_{60}N_6$. The optical properties, microstructure and thermal stability of this coating were investigated in detail.

2. Experimental

The Cu, $Zr_{0.3}Al_{0.7}N$, $Zr_{0.2}Al_{0.8}N$, $Al_{34}O_{60}N_6$ films and $Cu/Zr_{0.3}Al_{0.7}N/Zr_{0.2}Al_{0.8}N/Al_{34}O_{60}N_6$ coating were deposited on Si(1 1 1) and glass (soda lime glass) substrates by ISB700 system. The substrates were ultrasonic cleaned with acetone, ethanol and deionized water for 10 min sequentially at room temperature. The single layer (Cu, $Zr_{0.3}Al_{0.7}N$, $Zr_{0.2}Al_{0.8}N$ and $Al_{34}O_{60}N_6$) deposited on glass (soda lime glass) was used to the optical analysis. The films and coatings were deposited on Si(1 1 1) was for studying microstructure and thermal stability. A copper target (99.99% purity), an aluminum target (99.999% purity) and a zirconium target (99.9% purity) were sputtered by argon ion generated by a Kaufman ion source. The reaction ion (nitrogen ion and oxygen ion) generated by a Kaufman ion source bomdarded the substrate to synthesize the $Zr_{1-x}Al_xN$ (x = 0.7, 0.8) and $Al_{34}O_{60}N_6$ sub-layers. In order to avoid the charge accumulation on the surface of insulation substrate (such as Si(1 1 1) or glass), neutral filament at exit of reaction ion source was use to neutralize the nitrogen or oxygen ion. The base pressure was 2.0×10^{-4} Pa. The detail parameters were listed in Table 1. The solar selective absorbing coating has to work under a good vacuum ($\sim 10^{-2}$ Pa) at high temperature (up to 380 °C when the heat exchange fluid is diathermic oil and up to 550 °C in the case of molten salt) according to the concentrated ratio of solar radiation [22]. Considering the temperature fluctuation during service, we confirmed the annealing temperature was 400 °C and 600 °C, respectively. The coating deposited on Si(1 1 1) substrate was used to carry out the annealing experiment in vacuum (5.0×10^{-2} Pa) ambient at 400 °C or 600 °C for different times.

The optical constants of Cu, $Zr_{0.3}Al_{0.7}N$, $Zr_{0.2}Al_{0.8}N$ and $Al_{34}O_{60}N_6$ films were measured by spectroscopic ellipsometry (Type: M-2000UI). Based on the optical constants of single layer, the reflectance spectra of the cermet coatings with four-layer structure were optimized and calculated by a commercial optical simulation programme (Version Name: TFCalc 3.5.6). The experimental reflective spectra at 0° angle incidence were measured by UV-vis-NIR spectrophotometer (Type: Hitachi U4100) with the wavelength range from 250 nm to 2500 nm. The reflectance in the range of 2.5–25 μm was measured by Fourier Transform Infrared (FTIR) spectrophotometer (Type: Vertex80). The total solar absorptance (α_{solar}) is calculated according to the following equation:

$$\alpha_{solar} = \frac{\int_{250}^{2500} I_{solar}(\lambda)(1 - R(\lambda))d\lambda}{\int_{250}^{2500} I_{solar}d\lambda} \quad (1)$$

where $R(\lambda)$ is the measured reflectance from 250 nm to 2500 nm, and $I_{solar}(\lambda)$ is the ASTM AM1.5D solar spectral irradiance, which is the reference after passing through the atmosphere 1.5 times.

Thermal emittance ($\varepsilon_{thermal}(T)$) at the specific temperature is determined by the formula as follow:

$$\varepsilon_{thermal}(T) = \frac{\int_0^{\infty} I_{blackbody}(\lambda)(1 - R(\lambda))}{\int_0^{\infty} I_{blackbody}(\lambda)d(\lambda)} \quad (2)$$

where $\varepsilon_{thermal}(T)$ is an emittance at the temperature T. In our paper, the temperature is 400 °C. $I_{blackbody}(\lambda)$ is the spectral radiation of black body at 400 °C according to the *Planck's radiation law*.

The microstructure of coatings is investigated by Transmission Electron Microscope (TEM, type: Tecnai G^2 F20). The TEM is equipped with a high-angle angular-dark-field (HAADF) detector, X-ray energy-dispersive spectrometer (EDS) systems. The element distribution in depth was measured by Auger Electron Spectroscopy (AES, type: ULVAC- PHI 700).

3. Results and discussion

Fig. 1 shows the refractive index (Fig. 1a) and extinction coefficient (Fig. 1b) of Cu, $Zr_{0.3}Al_{0.7}N$, $Zr_{0.2}Al_{0.8}N$ and $Al_{34}O_{60}N_6$ films. The refractive index of Cu film shows the minimum at ~600 nm, thereafter it increases with wavelength, where extinction coefficient increases monotonically in the whole wavelength range. Additionally, the extinction coefficient value of Cu films is much higher than that of the others. Those results indicate the purely metallic behavior because the Cu film has high absorption in the IR range due to the phonon collision and free electron absorption. In the case of $Zr_{0.3}Al_{0.7}N$ film, the increase of refractive index and extinction coefficient indicates the metal-like behavior. For $Zr_{0.2}Al_{0.8}N$ film, refractive index reaches the maximum at the wavelength of ~320 nm, thereafter it decreases. Extinction coefficient decreases monotonically, and the extinction coefficient value is between 0.2 and 1.15 in the whole wavelength range. Those results reveal the intermediate behavior (i.e., between metallic and dielectric). Both refractive index and extinction coefficient of $Al_{34}O_{60}N_6$ film decrease with wavelength. The extinction value is almost zero, which displays

Table 1
The detail deposition parameters of $Cu/Zr_{0.3}Al_{0.7}N/Zr_{0.2}Al_{0.8}N/Al_{34}O_{60}N_6$ coating.

Materials	Target	Ar (sccm)	N_2 (sccm)	O_2 (sccm)	AIE (keV)	AIC (mA)	ASIE (eV)	ASIC (mA)	Time (min)
$Al_{34}O_{60}N_6$	Al	5	2	4	2.7	100	200	50	15
$Zr_{0.2}Al_{0.8}N$	Al	5	6		2.7	100	200	50	2.5
	Zr	5			2.7	40			
$Zr_{0.3}Al_{0.7}N$	Al	5	6		2.7	100	200	50	13.5
	Zr	5			2.7	60			
Cu	Cu	5	6		2.7	100	200	30	10
	Cu	5			2.7	100	0	0	10

AIE, AIC, ASIE, and ASIC correspond to argon ion energy, argon ion current, assisted ion energy and assisted ion current.

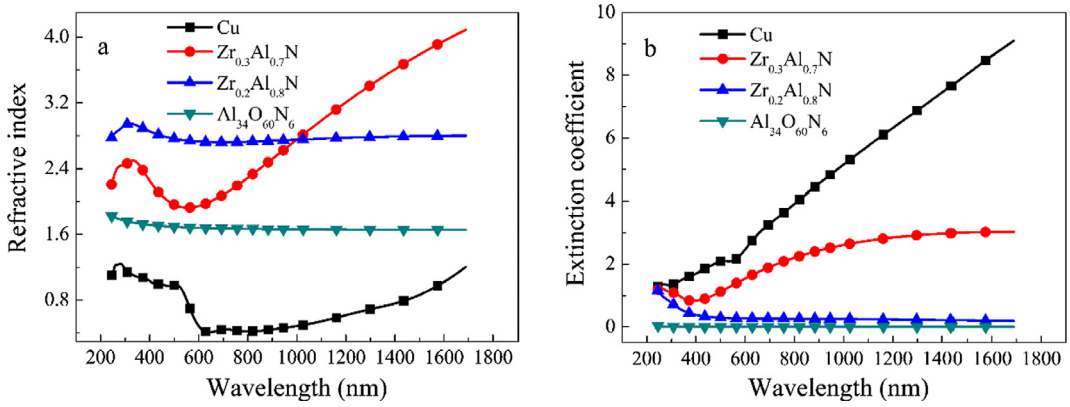

Fig. 1. Optical constants of Cu, $Zr_{0.3}Al_{0.7}N$, $Zr_{0.2}Al_{0.8}N$ and $Al_{34}O_{60}N_6$ films.

the dielectric behavior in nature. The low refractive index contributes to the low front surface reflections ($n_{550\ nm}$ = 1.69; R = 6.6%). It indicates the deposited $Al_{34}O_{60}N_6$ film is a good candidate of anti-reflection layer.

A schematic diagram of the Cu/$Zr_{0.3}Al_{0.7}N$/$Zr_{0.2}Al_{0.8}N$/$Al_{34}O_{60}N_6$ cermet coating and corresponding to reflectance spectra of theoretical and experimental are displayed in Fig. 2. From bottom to top, the optimized thickness of Cu, $Zr_{0.3}Al_{0.7}N$, $Zr_{0.2}Al_{0.8}N$ and $Al_{34}O_{60}N_6$ is 100 nm, 65 nm, 15 nm and 70 nm, respectively. Based on the optimized results, the Cu/$Zr_{0.3}Al_{0.7}N$/$Zr_{0.2}Al_{0.8}N$/$Al_{34}O_{60}N_6$ cermet coating with approximately optimized thickness was deposited on Si(1 1 1) and glass. From the reflectance spectra of theoretical and experimental in Fig. 2, we can find that the experiment reflectance agrees well with the theoretical reflectance. The deposited coatings exhibit low reflectance (<4%) in 450–1200 nm region (the concentration area of solar radiation energy) and high reflectance in the wavelength range of 2.5–25 μm (near infrared and infrared region). The reflectance in the visible region is close to zero, which is contributed to the instinct absorption of the double-cermet layer and the destructive interference effects [6,23]. The change from low to high reflectance abruptly occurred near 1000 nm. The sharp reflectance transition from solar spectra to the infrared wavelength range indicates the deposited coatings have the excellent properties of selective absorbing even at high temperature. According to the whole reflectance from 300 nm to 28,800 nm, the calculated solar absorptance is 0.953 and the thermal emittance is 0.079 at 400 °C.

The structure of deposited coatings was studied by TEM method. The thickness of sub-layer is measured in the TEM cross section of as-deposited coating. The thickness of as-deposited sub-layer is close to the designed thickness value, particularly for the $Zr_{0.3}Al_{0.7}N$ and $Zr_{0.2}Al_{0.8}N$ films. The slight deviation of $Al_{34}O_{60}N_6$ film between designed and deposited value cause the slight deviation between theoretical and experimental reflectance in the wavelength from 250 nm to 2500 nm. Those results indicate the obtained optical constants is credible deposited process have high controllability. The SAED image of $Zr_{0.3}Al_{0.7}N$, $Zr_{0.2}Al_{0.8}N$ and $Al_{34}O_{60}N_6$ is displayed in Fig. 3b. Table 2 gives a diffraction ring analysis in terms of the corresponding phase and d-spacing. Three diffraction roles (r_1, r_2, r_3) can be observed. After measured precisely and calibrated, the measured d-spacing (r_1) of 0.2478 nm can be indexed as h-AlN(0 0 2) reflection (PDF database file 65-0832). The measured d-spacing from the diffraction role of r_2 and r_3 shows that the interplanar distances of d_2 (0.2205 nm) and d_3 (0.156 nm) are assigned to the panels of c-ZrN(2 0 0) and c-ZrN (2 2 0) (PDF database file 02-0956). The measured d-spacing deviation the theoretical value is due to the substitution of zirconium atoms by aluminum atom which has the smaller atom radius than the atom radius of zirconium [24]. The diffraction role of h-AlN(0 0 2) is diffused and not sharp, which indicates the content of crystalline phase is less and the crystallinity is poor. In order to analyze the microstructure of single sub-layer, the HRTEM analysis of the single sub-layer is carried out. The crystalline phase of h-AlN and c-ZrAlN can be observed in the $Zr_{0.3}Al_{0.7}N$ sub-layer (Fig. 3c). Additionally, a little of amorphous phase can also be noted in the zone A. For the $Zr_{0.2}Al_{0.8}N$ and $Al_{34}O_{60}N_6$ sub-layer, the amorphous structure is confirmed in the Fig. 3d. Based on the above results, the diffraction roles are from the crystalline phase in the $Zr_{0.3}Al_{0.7}N$ sub-layer.

The Gibbs energy of the formation of ZrN at 298 K ($\Delta G^{\theta}_{ZrN} = -344.0$ kJ/mol) [25] is lower than that of AlN ($\Delta G^{\theta}_{AlN} = -287.0$ kJ/mol) [26]. So, the nitrogen atoms arriving at the substrate surface are inclined to combine with zirconium atoms and synthesize the ZrN easily. Then, aluminum atom

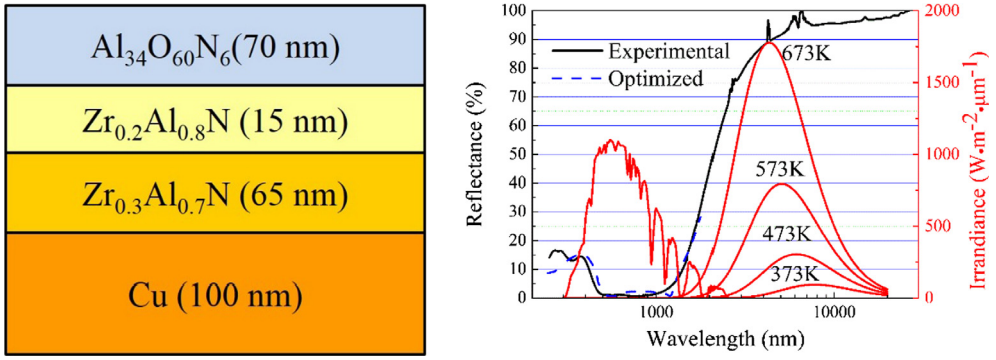

Fig. 2. Schematic diagram of the Cu/$Zr_{0.3}Al_{0.7}N$/$Zr_{0.2}Al_{0.8}N$/$Al_{34}O_{60}N_6$ absorber coating and corresponding to optimized theoretical and experimental reflectance spectra.

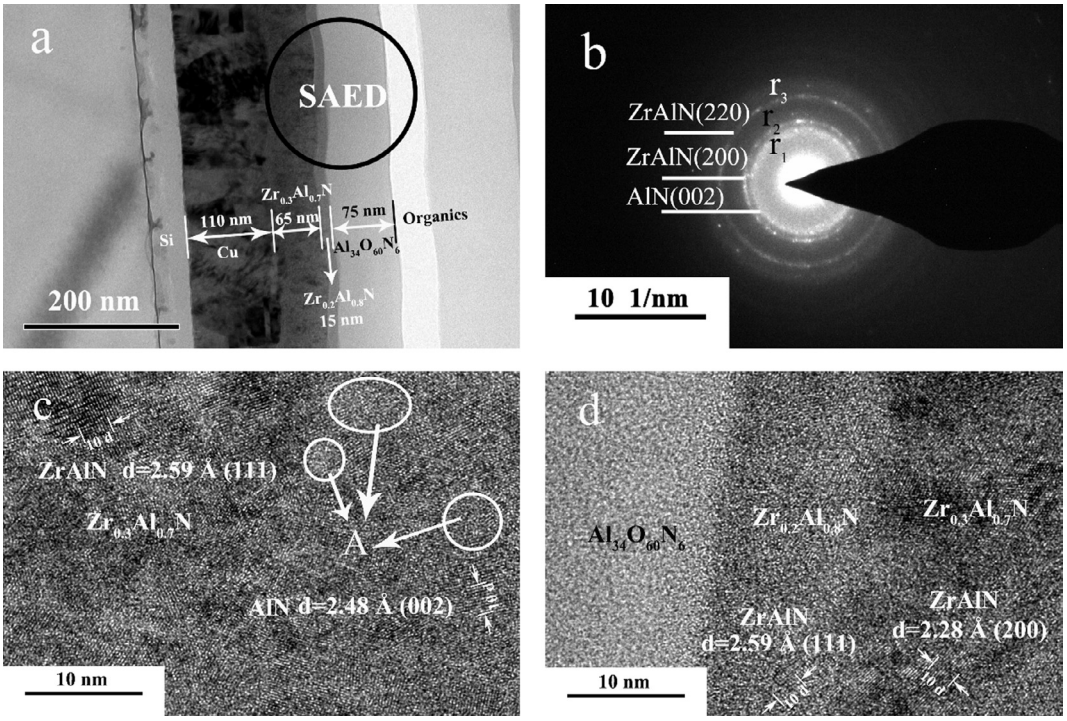

Fig. 3. The TEM analysis of as-deposited coatings, (a) TEM cross section of Cu/$Zr_{0.3}Al_{0.7}N$/$Zr_{0.2}Al_{0.8}N$/$Al_{34}O_{60}N_6$ coating, (b) SAED image of $Zr_{0.3}Al_{0.7}N$/$Zr_{0.2}Al_{0.8}N$/$Al_{34}O_{60}N_6$ layer corresponding to the area in the image of a, (c) HRTEM image of $Zr_{0.3}Al_{0.7}N$ sub-layer, (d) HRTEM image of $Zr_{0.3}Al_{0.7}N$/$Zr_{0.2}Al_{0.8}N$/$Al_{34}O_{60}N_6$ interface.

Table 2
The detail information of diffraction role for as-deposited Cu/$Zr_{0.3}Al_{0.7}N$/$Zr_{0.2}Al_{0.8}N$/$Al_{34}O_{60}N_6$ coating.

Determination of diffraction rings			Phase calibration			Phase
Ring No.	nm^{-1}	Measured *d*-spacing (nm)	Standard *d*-spacing (nm)	*h k l*	Standard phase	
r_1	4.0217	0.2486	0.249	(0 0 2)	*h*-AlN	*h*-AlN
r_2	4.5353	0.2205	0.229	(2 0 0)	*c*-ZrN	*c*-ZrAlN
r_3	6.4103	0.1560	0.162	(2 2 0)	*c*-ZrN	

replaces the zirconium atom to form the $Zr_{1-x}Al_xN$ solid solution. In the case of $Zr_{0.3}Al_{0.7}N$ sub-layer, high zirconium composition is benefit to the crystal nucleus growth of ZrAlN. The formation of AlN crystal phase is related to the thermodynamic and kinetic factors. For the thermodynamic factor, the metastable *c*-AlN and stable *c*-ZrN have the same structure. The lattice constant of *c*-AlN and *c*-ZrN is 0.412 nm (PDF database file 25-1495) and 0.456 nm (PDF database 02-0956). What's more, the lattice constant of *c*-ZrAlN decreases due to the zirconium atom is replaced with aluminum atom, which decreases the mismatch degree further. The *c*-AlN can be formed on the *c*-ZrAlN substrate as the coherent growth due to template effect to decrease the free energy of system [27]. For the vapor deposition, it is well known that the most important kinetic factor is the mobility of the deposited particles [28]. Generally, the particles have high mobility in the surface of the heterogeneous material. With the *c*-AlN thickness increase, the strain energy increases, which results in the system free energy increase. The *c*-AlN does not grow as the coherent interface, and it transforms into the non-coherent interface. Without the template effect, the metastable *c*-AlN will transform into the stable *h*-AlN [29,30]. The $Zr_{0.3}Al_{0.7}N$ sub-layer is mainly composed of *c*-ZrAlN and *h*-AlN with little amorphous. For the $Zr_{0.2}Al_{0.8}N$ sub-layer, the crystal nucleus cannot grow into grain due to the low content of zirconium atom. The crystallinity of $Al_{34}O_{60}N_6$ is poor. Hence, the sub-layers of $Zr_{0.2}Al_{0.8}N$ and $Al_{34}O_{60}N_6$ are amorphous.

The annealing experiment was performed in a vacuum ambient (5.0×10^{-2} Pa) using a tubular furnace. Table 3 gives the absorptance and emittance change of the annealed coatings. The absorptance and emittance of the coating after annealing treatment at

Table 3
Effect of annealing temperature and time on absorptance and emittance of Cu/$Zr_{0.3}Al_{0.7}N$/$Zr_{0.2}Al_{0.8}N$/$Al_{34}O_{60}N_6$ coating.

Condition	As-deposited	400 °C 96 h	400 °C 144 h	400 °C 168 h	400 °C 192 h
Absorptance (α)	0.953	0.952	0.953	0.952	0.952
Emittance ($\varepsilon_{400\ °C}$)	0.079	0.078	0.080	0.077	0.074
α/ε	12.1	12.2	11.9	12.4	12.9
Condition	As-deposited	600 °C 96 h	600 °C 144 h	600 °C 168 h	600 °C 192 h
Absorptance (α)	0.953	0.956	0.959	0.958	0.963
Emittance ($\varepsilon_{400\ °C}$)	0.079	0.092	0.108	0.119	0.141
α/ε	12.1	10.4	8.88	8.05	6.86

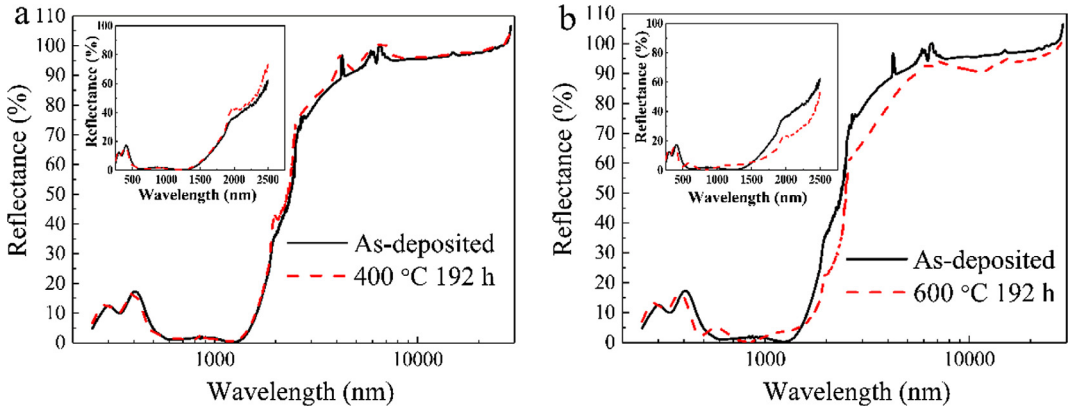

Fig. 4. Reflectance spectra of as-deposited and annealed coatings, (a) as-deposited (black solid line) and after (red dashed line) annealing at 400 °C for 192 h, (b) as-deposited (black solid line) and after (red dashed line) annealing at 600 °C for 192 h. (For interpretation of the references to colour in this figure legend, the reader is referred to the web version of this article.)

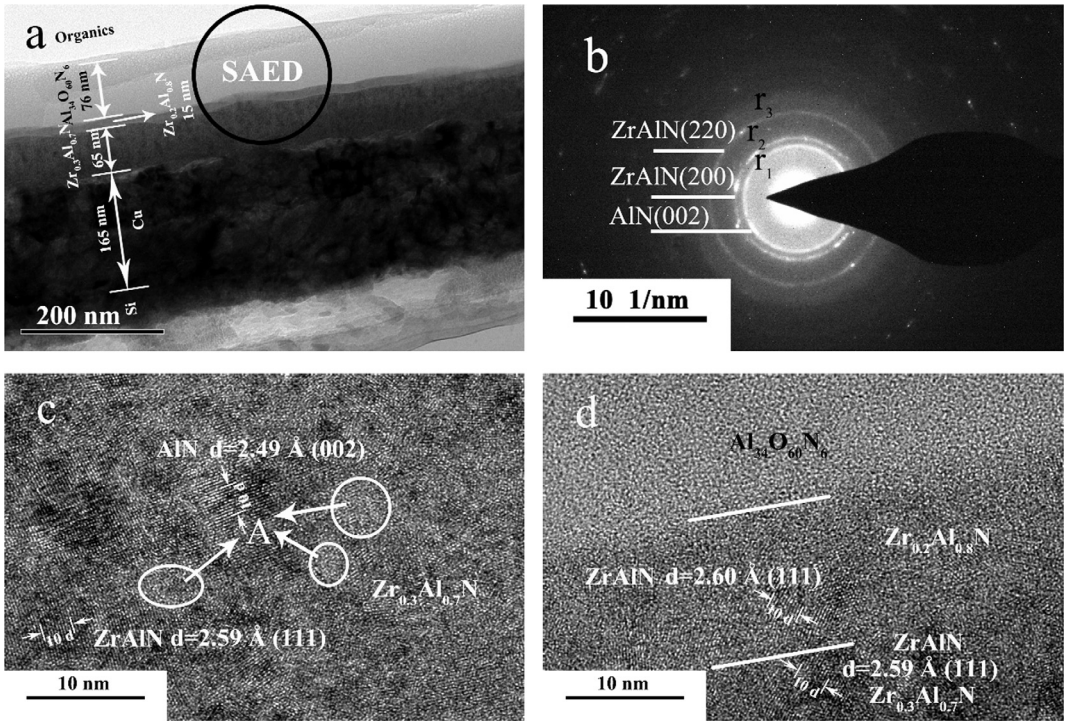

Fig. 5. The TEM analysis of annealed coating, (a) TEM cross section of Cu/$Zr_{0.3}Al_{0.7}N$/$Zr_{0.2}Al_{0.8}N$/$Al_{34}O_{60}N_6$ coatings, (b) SAED image of $Zr_{0.3}Al_{0.7}N$/$Zr_{0.2}Al_{0.8}N$/$Al_{34}O_{60}N_6$ layer corresponding to the area in the image of a, (c) HRTEM image of $Zr_{0.3}Al_{0.7}N$ sub-layer, (d) HRTEM image of $Zr_{0.3}Al_{0.7}N$/$Zr_{0.2}Al_{0.8}N$/$Al_{34}O_{60}N_6$ interface.

400 °C is almost stable. No significant change of reflectance between as-deposited coating and annealed coating for 192 h at 400 °C is noted in Fig. 4a. Those results indicate the prepared coatings have high thermal stability at 400 °C. In the case of the coating after annealing treatment at 600 °C, absorptance slightly increases with time increase, whereas, emittance increases obviously. The photothermal conversion efficient (α/ε) decreases from 12.1 to 6.86. The spectral reflectance below ~1500 nm increases slightly while it decreases above ~1500 nm.

The microstructure of coating after annealing at 600 °C for 192 h was investigated by TEM. Fig. 5a shows the TEM cross section of the coating after annealing at 600 °C. Compared with TEM cross-section of as-deposited coating, the thickness of the $Zr_{0.3}Al_{0.7}N$, $Zr_{0.2}Al_{0.8}N$ and $Al_{34}O_{60}N_6$ sub-layer keeps stable, whereas, the interface become obscure. It indicates the element diffusion is taken place at the interface. The thickness of Cu infrared layer become thicker compared to the pristine coating, indicating serious element diffusion between Si(1 1 1) substrate and Cu sub-layer. The SAED pattern for as-deposited and annealed coatings have the same characterization. Table 4 gives a detail information of phase analysis. For the absorbing and anti-reflection layer (including $Zr_{0.3}Al_{0.7}N$, $Zr_{0.2}Al_{0.8}N$ and $Al_{34}O_{60}N_6$ layer), it also contains *h*-AlN and *c*-ZrAlN phase. However, the diffraction role corresponding to the *h*-AlN(0 0 2) becomes sharp, concentrated and brighter (as shown in Fig. 5b). It manifests the *h*-AlN phase increases after annealing treatment. To further confirm the microstructure of sub-layer, the HRTEM analysis was implemented. The $Zr_{0.3}Al_{0.7}N$ sub-layer is mainly composed of *h*-AlN and *c*-ZrAlN with little amorphous (zone A). The $Zr_{0.2}Al_{0.8}N$ sub-layer consists of amorphous and little *c*-ZrAlN phase. The

Table 4
The detail information of diffraction role for $Cu/Zr_{0.3}Al_{0.7}N/Zr_{0.2}Al_{0.8}N/Al_{34}O_{60}N_6$ coating after annealing treatment for 192 at 600 °C in vacuum.

Determination of diffraction rings			Phase calibration			Phase
Ring No.	nm^{-1}	Measured *d*-spacing (nm)	Standard *d*-spacing (nm)	*h k l*	Standard phase	
r_1	4.0541	0.2467	0.248	(0 0 2)	*h*-AlN	*h*-AlN
r_2	4.4836	0.2230	0.229	(2 0 0)	*c*-ZrN	*c*-ZrAlN
r_3	6.3913	0.1565	0.162	(2 2 0)	*c*-ZrN	

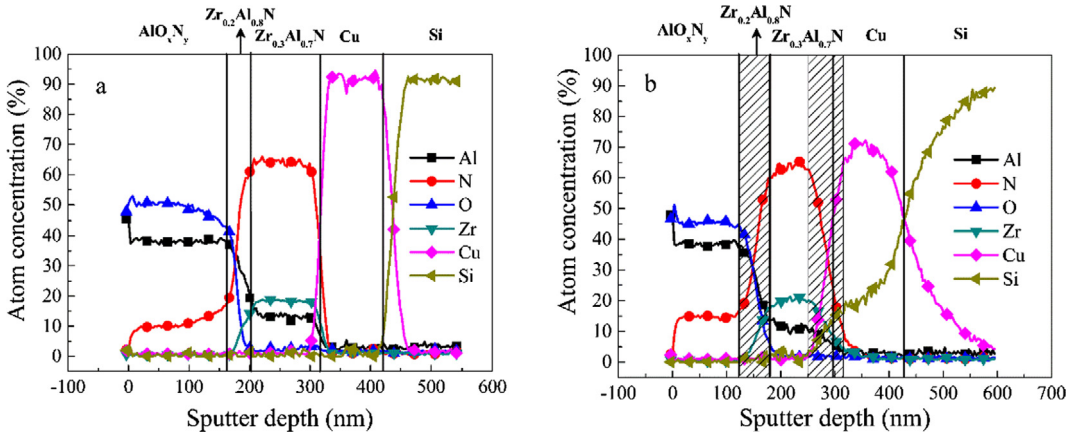

Fig. 6. Depth profile of as-deposited and annealed $Cu/Zr_{0.3}Al_{0.7}N/Zr_{0.2}Al_{0.8}N/Al_{34}O_{60}N_6$ coatings, (a) as-deposited, (b) annealing treatment at 600 °C for 192 h.

$Al_{34}O_{60}N_6$ anti-reflection layer is amorphous. From above results and analysis, we can confirm that *h*-AlN phase increases in $Zr_{0.3}Al_{0.7}N$ sub-layer.

The element distribution of as-deposited and annealed coating was analyzed by AES. For element distribution of as-deposited (As shown in Fig. 6a), the sub-layer can be distinguished clearly. Around interface, the atom concentration rises or drops sharply. After annealing treatment at 600 °C for 192 h (as shown in Fig. 6b), the sub-layer of Cu, $Zr_{0.3}Al_{0.7}N$, $Zr_{0.2}Al_{0.8}N$ and $Al_{34}O_{60}N_6$ can also be found correspondingly, whereas, the change of atom concentration at interface become gently (see the shaded zone in Fig. 6b). It is noteworthy that nitrogen element in the $Zr_{0.3}Al_{0.7}N$ films diffuses toward Cu and $Zr_{0.2}Al_{0.8}N$ sub-layer terrible. The diffusion between and Si(1 1 1) and Cu sub-layer is also serious.

In the Me-Al-N system (Me = Ti, Zr and Hf and so on), the MeAlN is metastable phase. Annealing treatment at high temperature, the *c*-ZrAlN phase will transform into the stable phases *c*-ZrN and metastable phase *c*-AlN by spinodal decomposition initially [31–35]. Then, the metastable phase of *c*-AlN will transform into the stable phase *h*-AlN finally [32]. During this process, the Al-N bond will break, which results in the escape and loss of nitrogen atom [36]. A schematic illustration of the *c*-AlN formation after annealing treatment at 600 °C for 192 h is showed in Fig. 7. The escaped nitrogen atoms can diffuse easily along to the grain boundary [37,38]. Those factors cause the serious diffusion of nitrogen atoms. In the case of the $Zr_{0.2}Al_{0.8}N$ sub-layer, the *c*-ZrAlN phase is little, additionally, amorphous at the interface can suppress the process of spinodal decomposition [39]. There is a serious diffusion between copper and silicon due to the low active energy of diffusion (0.43 eV) and interstitial diffusion [40,41]. The diffusion coefficient between copper and silicon is high. Additionally, high temperature accelerates the diffusion process. Those factors lead

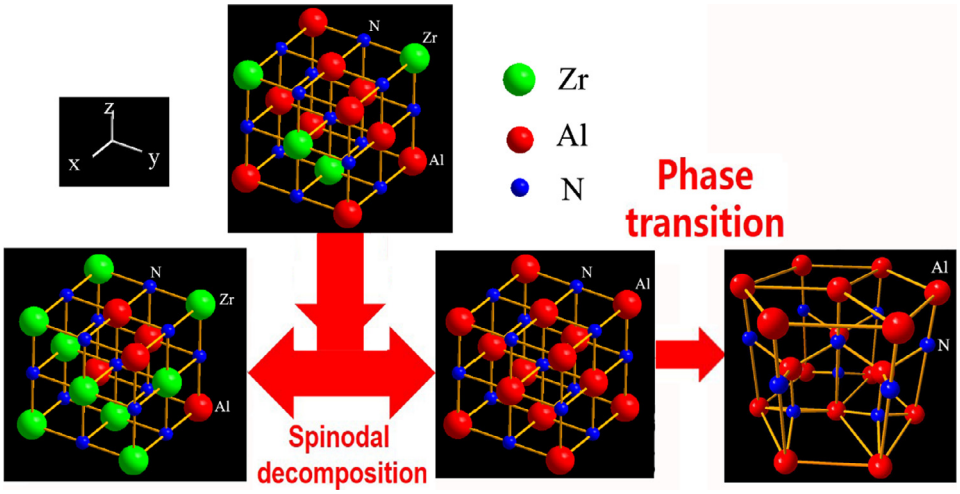

Fig. 7. Schematic illustration of the AlN formation after annealing treatment at 600 °C for 192 h.

to the serious diffusion between copper and silicon. Based on the knowledge of solid state physics, the infrared reflectance is positively correlated with the number of free electrons. The Cu_3Si, Cu_5Si and $Cu_{15}Si_4$ compound will be formed during the diffusion process between copper and silicon [42,43], which will decrease the number of free electrons. It decreases the infrared reflection and increases the emittance of coatings.

4. Conclusion

The high-performance $Cu/Zr_{0.3}Al_{0.7}N/Zr_{0.2}Al_{0.8}N/Al_{34}O_{60}N_6$ cermet coating has been successfully prepared by ion beam assisted deposition. The experimentally deposited coating achieves the high absorptance of 0.953 and the low emittance of 0.079 at 400 °C. Annealing experiment at 400 °C in vacuum indicates the deposited coating exhibits the excellent thermal stability. After annealing treatment at 600 °C, the photothermal conversion efficient decrease from 12.1 to 6.86 owing to the emittance increase. The spinodal decomposition of the metastable *c*-ZrAlN phase in the $Zr_{0.3}Al_{0.7}N$ sub layer and the phase transition from *c*-AlN to *h*-AlN contribute to the nitrogen diffusion, which leads to the composition of the $Zr_{0.3}Al_{0.7}N$ sub-layer deviates the initial design after annealing treatment. Additionally, the serious diffusion between copper and silicon substrate also increases the emittance of coating. The phenomenon that nitrogen diffusion is caused by spinodal decomposition and phase transition is a valuable discovery for the thermal-stability improvement of cermet-based solar selective absorbing coatings.

Acknowledgments

This work was supported by Program of China (Grant No. 2015BAA02B04) under the Ministry of Science and Technology of China, NSFC (31571006) and "Thousands Talents" program for pioneer researcher and his innovation team.

References

[1] N.S. Lewis, Toward cost-effective solar energy use, Science 315 (2007) 798–801.
[2] N.S. Lewis, Research opportunities to advance solar energy utilization, Science 351 (2016) aad1920.
[3] H. Price, E. Lupfert, D. Kearney, E. Zarza, G. Cohen, R. Gee, R. Mahoney, Advances in parabolic trough solar power technology, J. Sol. Energy Eng. 124 (2002) 109–125.
[4] C.G. Granqvist, Solar energy materials, Adv. Mater. 15 (2003) 1789–1803.
[5] M. Farooq, M. Hutchins, Optical properties of higher and lower refractive index composites in solar selective coatings, Sol. Energy Mater. Sol. Cells 71 (2002) 73–83.
[6] Q.C. Zhang, D.R. Mills, Very low-emittance solar selective surfaces using new film structures, J. Appl. Phys. 72 (1992) 3013–3021.
[7] A. Biswas, D. Bhattacharyya, H.C. Barshilia, N. Selvakumar, K. Rajam, Spectroscopic ellipsometric characterization of $TiAlN/TiAlON/Si_3N_4$ tandem absorber for solar selective applications, Appl. Surf. Sci. 254 (2008) 1694–1699.
[8] Q.-C. Zhang, D.R. Mills, High solar performance selective surface using bi-sublayer cermet film structures, Sol. Energy Mater. Sol. Cells 27 (1992) 273–290.
[9] S. Zhao, C.-G. Ribbing, E. Wäckelgård, Optical constants of sputtered Ni/NiO solar absorber film—depth-profiled characterization, Sol. Energy Mater. Sol. Cells 84 (2004) 193–203.
[10] L. Gaouyat, F. Mirabella, O. Deparis, Critical tuning of magnetron sputtering process parameters for optimized solar selective absorption of $NiCrO_x$ cermet coatings on aluminium substrate, Appl. Surf. Sci. 271 (2013) 113–117.
[11] L. Zheng, F. Gao, S. Zhao, F. Zhou, J.P. Nshimiyimana, X. Diao, Optical design and co-sputtering preparation of high performance $Mo–SiO_2$ cermet solar selective absorbing coating, Appl. Surf. Sci. 280 (2013) 240–246.
[12] M. Veszelei, K. Andersson, C.-G. Ribbing, K. Järrendahl, H. Arwin, Optical constants and Drude analysis of sputtered zirconium nitride films, Appl. Opt. 33 (1994) 1993–2001.
[13] H.C. Barshilia, N. Selvakumar, K. Rajam, D. Sridhara Rao, K. Muraleedharan, A. Biswas, $TiAlN/TiAlON/Si_3N_4$ tandem absorber for high temperature solar selective applications, Appl. Phys. Lett. 89 (2006) 191909.
[14] K. Zhang, M. Du, L. Haoa, J. Meng, J. Wang, J. Mi, X. Liu, Highly corrosion resistant and sandwich-like $Si_3N_4/Cr-CrN_x/Si_3N_4$ coatings used for solar selective absorbing applications, ACS Appl. Mater. Interfaces 8 (2016) 34008–34018.
[15] J.-P. Meng, X.-P. Liu, Z.-Q. Fu, K. Zhang, Optical design of $Cu/Zr_{0.2}AlN_{0.8}/ZrN/AlN/ZrN/AlN/Al_{34}O_{62}N_4$ solar selective absorbing coatings, Sol. Energy 146 (2017) 430–435.
[16] N. Selvakumar, N. Manikandanath, A. Biswas, H.C. Barshilia, Design and fabrication of highly thermally stable $HfMoN/HfON/Al_2O_3$ tandem absorber for solar thermal power generation applications, Sol. Energy Mater. Sol. Cells 102 (2012) 86–92.
[17] Y. Wu, C. Wang, Y. Sun, Y. Xue, Y. Ning, W. Wang, S. Zhao, E. Tomasella, A. Bousquet, Optical simulation and experimental optimization of $Al/NbMoN/NbMoON/SiO_2$ solar selective absorbing coatings, Sol. Energy Mater. Sol. Cells 134 (2015) 373–380.
[18] L. Wu, J. Gao, Z. Liu, L. Liang, F. Xia, H. Cao, Thermal aging characteristics of CrN_xO_y solar selective absorber coating for flat plate solar thermal collector applications, Sol. Energy Mater. Sol. Cells 114 (2013) 186–191.
[19] H.C. Barshilia, N. Selvakumar, K. Rajam, Thermal stability of $TiAlN/TiAlON/Si_3N_4$ tandem absorbers prepared by reactive direct current magnetron sputtering, J. Vacuum Sci. Technol. A: Vacuum, Surfaces, Films 25 (2007) 383–390.
[20] A. Rizzo, M. Signore, D. Valerini, D. Altamura, A. Cappello, L. Tapfer, A study of suppression effect of oxygen contamination by bias voltage in reactively sputtered ZrN films, Surf. Coat. Technol. 206 (2012) 2711–2718.
[21] H. Al-Shareef, X. Chen, D. Lichtenwalner, A. Kingon, Analysis of the oxidation kinetics and barrier layer properties of ZrN and Pt/Ru thin films for DRAM applications, Thin Solid Films 280 (1996) 265–270.
[22] A. Antonaia, A. Castaldo, M. Addonizio, S. Esposito, Stability of $W-Al_2O_3$ cermet based solar coating for receiver tube operating at high temperature, Sol. Energy Mater. Sol. Cells 94 (2010) 1604–1611.
[23] F. Cao, D. Kraemer, T. Sun, Y. Lan, G. Chen, Z. Ren, Enhanced thermal stability of $W-Ni-Al_2O_3$ cermet-based spectrally selective solar absorbers with tungsten infrared reflectors, Adv. Energy Mater. 5 (2015).
[24] J.-P. Meng, K. Zhang, X.-P. Liu, Z.-Q. Fu, Z. Li, Influence of the aluminum content on structure and optical properties of $Zr_{1-x}Al_xN$ films, Vacuum 145 (2017) 268–271.
[25] W.-E. Wang, D.R. Olander, Computational thermodynamics of the Zr-N system, J. Alloys Compounds 224 (1995) 153–158.
[26] B.-Y. Shew, J.-L. Huang, The effects of nitrogen flow on reactively sputtered TiAlN films, Surf. Coat. Technol. 71 (1995) 30–36.
[27] A. Madan, I. Kim, S. Cheng, P. Yashar, V. Dravid, S. Barnett, Stabilization of cubic AlN in epitaxial AlN/TiN superlattices, Phys. Rev. Lett. 78 (1997) 1743.
[28] Z. Zhang, M.G. Lagally, Atomistic processes in the early stages of thin-film growth, Science 276 (1997) 377–383.
[29] D. Holec, R. Rachbauer, L. Chen, L. Wang, D. Luef, P.H. Mayrhofer, Phase stability and alloy-related trends in Ti–Al–N, Zr–Al–N and Hf–Al–N systems from first principles, Surf. Coat. Technol. 206 (2011) 1698–1704.
[30] S. Sheng, R. Zhang, S. Veprek, Phase stabilities and thermal decomposition in the $Zr_{1-x}Al_xN$ system studied by ab initio calculation and thermodynamic modeling, Acta Mater. 56 (2008) 968–976.
[31] J.W. Cahn, On spinodal decomposition, Acta Metall. 9 (1961) 795–801.
[32] P.H. Mayrhofer, L. Hultman, J.M. Schneider, P. Staron, H. Clemens, Spinodal decomposition of cubic $Ti_{1-x}Al_xN$: comparison between experiments and modeling, Int. J. Mater. Res. 98 (2007) 1054–1059.
[33] L. Rogström, M. Johansson, N. Ghafoor, L. Hultman, M. Odén, Influence of chemical composition and deposition conditions on microstructure evolution during annealing of arc evaporated ZrAlN thin films, J. Vacuum Sci. Technol. A: Vacuum, Surfaces, Films 30 (2012) 031504.
[34] R. Sanjinés, C. Sandu, R. Lamni, F. Lévy, Thermal decomposition of $Zr_{1-x}Al_xN$ thin films deposited by magnetron sputtering, Surf. Coat. Technol. 200 (2006) 6308–6312.
[35] L. Rogström, L. Johnson, M. Johansson, M. Ahlgren, L. Hultman, M. Odén, Thermal stability and mechanical properties of arc evaporated ZrN/ZrAlN multilayers, Thin Solid Films 519 (2010) 694–699.
[36] M. Moser, D. Kiener, C. Scheu, P.H. Mayrhofer, Influence of yttrium on the thermal stability of Ti-Al-N thin films, Materials 3 (2010) 1573–1592.
[37] S. Yue, S. Yueyan, W. Fengchun, High-temperature optical properties and stability of Al_xO_y-AlN_x-Al solar selective absorbing surface prepared by DC magnetron reactive sputtering, Sol. Energy Mater. Sol. Cells 77 (2003) 393–403.
[38] J.-P. Meng, X.-P. Liu, Z.-Q. Fu, X.-J. Wang, L. Hao, Thermal stability of AlN films prepared by ion beam assisted deposition, Appl. Surf. Sci. 347 (2015) 109–115.
[39] S. Veprek, H.-D. Männling, M. Jilek, P. Holubar, Avoiding the high-temperature decomposition and softening of $(Al_{1-x}Ti_x)$ N coatings by the formation of stable superhard nc-$(Al_{1-x}Ti_x)$ N/a-Si_3N_4 nanocomposite, Mater. Sci. Eng. A 366 (2004) 202–205.
[40] R. Hall, J.H. Racette, Diffusion and solubility of copper in extrinsic and intrinsic germanium, silicon, and gallium arsenide, J. Appl. Phys. 35 (1964) 379–397.
[41] J. Poate, D. Jacobson, J. Williams, R. Elliman, D. Boerma, Diffusion of implanted impurities in amorphous Si, Nucl. Instrum. Methods Phys. Res., Sect. B 19 (1987) 480–483.
[42] R. Chromik, W. Neils, E. Cotts, Thermodynamic and kinetic study of solid state reactions in the Cu–Si system, J. Appl. Phys. 86 (1999) 4273–4281.
[43] S.Q. Hong, C.M. Comrie, S.W. Russell, J.W. Mayer, Phase formation in Cu-Si and Cu-Ge, J. Appl. Phys. 70 (1991) 3655–3660.